Spatially Resolved UV Spectra of the High-Velocity Nuclear Outflow of NGC 1068[1]

Brent A. Groves

Research School of Astronomy & Astrophysics, Australian National University, Cotter Road, Weston Creek, ACT 2611 Australia

bgroves@mso.anu.edu.au

Gerald Cecil

Dept. of Physics & Astronomy, University of North Carolina at Chapel Hill, Chapel Hill, NC, USA 27599-3255

Pierre Ferruit

Observatoire de Lyon, 9 Avenue Charles Andre, Saint-Genis, Laval Cedex F-69561, France

Michael A. Dopita

Research School of Astronomy & Astrophysics, Australian National University, Cotter Road, Weston Creek, ACT 2611 Australia

ABSTRACT

We present UV emission-line maps of the NLR of NGC 1068. The maps span $\lambda\lambda$115–318 nm, the biconical ionization cone, a few potential jet/ISM interactions, and the compact knots whose optical spectra we reported previously bear strong kinematical resemblance to quasar Associated Absorption Line systems. Across the NLR, UV flux ratios are consistent with photoionization, not shock excitation, even for gas blueshifted abruptly to 3000 $\mathrm{km\,s^{-1}}$ relative to galaxy systemic velocity or for gas projected on the radio jet. The knots may be radiatively accelerated, photoablated fragments of molecular clouds.

Subject headings: galaxies: active — galaxies: individual (NGC 1068) — galaxies: kinematics & dynamics — galaxies: Seyfert

---

1. Introduction

While broad emission line profiles are a characteristic signature of the energetic processes in the center of active galaxies, the spectra of some systems also show absorption lines. Such absorption is generally found against the UV continuum, where the line profiles can extend blueward of galaxy systemic velocity from a few hundred to several thousand $km\,s^{-1}$ (Hamann et. al. 1997). Whereas the properties of the emission line clouds are reasonably well understood, less is known about the absorbing gas, especially how it is accelerated to such high velocities. The main problem in understanding such systems is that the background continuum necessary for absorption in active galaxies is often present only at the nucleus and at distributed, compact "hot spots".

Space telescopes permit the study of active galaxies with much better spatial resolution and at UV wavelengths. Such a study on carefully selected nearby systems can clarify both the background against which the absorbers are seen, and — the subject of this paper — the connection between the emitting and the absorbing complexes. In Cecil et al. (2002, hereafter Paper I) we reported on results derived from a grid of Space Telescope Imaging Spectrograph (STIS) medium resolution spectra that cover much of the spatially extended narrow line region (NLR) emission of the nearby Seyfert galaxy NGC 1068. As Figure 1 shows, we found that many compact "knots" in this NLR span velocities greater than 3000 $km\,s^{-1}$ in radial velocity, and are consistently blueshifted from galaxy systemic. The profiles of optical spectral lines from these knots resemble those of associated absorption line (AAL) systems seen in some quasar spectra. Using combined ground–based optical/IR and UV emission-line spectra, we can constrain the internal physical properties of these objects. In this paper we discuss the UV spectra.

UV spectra are potentially more sensitive probes of NLR conditions than lines in the visible because their collisionally excited lines are strong when emitted from the cooling region behind high-velocity $(150-500\ km\,s^{-1})$ shocks. Allen, Dopita, & Tsvetanov (1998, ADT herafter) showed that UV emission-line flux ratios can even discriminate between the two major excitation mechanisms posited for NLRs: shock fronts moving at $\lesssim 400\ km\,s^{-1}$ with photoionized precursors, and gas that has been photoionized by the AGN non-stellar continuum. In practice, UV spectra have been of limited use because mapping NLR's is slow with current space spectrometers, and the emission is easily extinguished by dust.

While NLR's are widely assumed to be photoionized structures, patterns of their internal motions suggest two means of gas acceleration: virial in the gravitational potential of the galaxy bulge (Nelson & Whittle 1996), and locally at the boundaries of expanding radio lobes (Axon et al. 1998, for example). Previous, sparsely sampled long-slit spectra of NGC 1068 (Axon et al. 1998; Kraemer & Crenshaw 2000) found discontinuities in the velocity field at several points that seem to coincide with excitation changes, suggesting to those authors a role for shocks near the radio jet. Grimes, Kriss, & Espey (1999) argue that shocks are responsible for the bright C IIIλ977 and N IIIλ991 emission in the off-nuclear *HUT* spectra. On the other hand, spatially resolved *XMM/Newton* spectra (Kinkhabwala et al. 2002) indicate that most of the X-ray emitting gas is

photoionized, not shocked excited.

In §2 we discuss the acquisition and reduction of the UV STIS low-resolution spectra, and register them to the medium resolution spectra discussed in Paper I. Our spectra span about 30% of the area of the NLR at high ($0\farcs05 = 3.5$ pc) spatial resolution, to better constrain the physical processes that operate there. In §3 we plot the emission line flux ratios in diagnostic diagrams to compare them to the predictions of different excitation models. In §4 we discuss the results in terms of the physical processes occuring in the high-velocity knots, and how these relate to Associated Absorption Line (AAL) systems in some quasar spectra. Our conclusions are summarized in §5. We assume that the distance and systemic velocity of NGC 1068 is 14.4 Mpc and $cz = 1148$ km s^{-1}.

2. Observations & Reductions

Seven UV spectra of NGC 1068 were recorded on the *HST* STIS/MAMA detectors: a pair of FUV+NUV exposures at three parallel slits placed along the axis of the radio jet, and a single NUV exposure at a fourth parallel position. Our observations were detailed in Table 1 of Paper I.

Figure 1 registers the STIS slits to the [O III] clouds and radio image (Gallimore, Baum, & O'Dea 1996), with UV spectra recorded at [O III] slit positions 2–4 (and 5 for the fourth NUV slit). These positions primarily sample the high-velocity, blueshifted knots discussed in Paper I, and secondarily sample gas on and adjacent to the radio jet. Time constraints prevented us from mapping parts of the NLR farther to the NW where there is optical or radio evidence for jet/ISM interactions, in particular at clouds B–C (see Gallimore, Baum, & O'Dea 1996), G (see Pécontal et al. 1997), and H (see Axon et al. 1998).

We chose the $0\farcs2$-wide slit ($0\farcs19$ on the sky) as a compromise between velocity resolution and spatial coverage. An important consideration for kinematical studies with STIS is that this slit projects to a width of 8 pixels on the MAMA detectors and produces [2] "triangular" wings on narrow emission lines that span 10 pixels. The UV PSF of the telescope within the STIS slit is much smaller than this width. Hence, compact emission knots at the same radial velocity will map to different wavelengths in the dispersed spectrum. STIS/MAMA dispersion is 0.6 Å and 1.58 Å FWHM in the G140L and G230L gratings used for FUV and NUV spectra, respectively. This implies maximum velocity shifts from nominal positions for two knots separated by the slit width of ±465 and ±375 km s^{-1}, respectively (see www.stsci.edu/hst/stis/design/gratings). These limits set the velocity resolution of our spectra because, lacking narrow-band images of the NLR in all spectral lines, we cannot map knots to specific locations across the slit. For our purposes, this "slit effect" uncertainty is tolerable because the components evident in the emission-line profiles in Figure 3 range over much larger velocities.

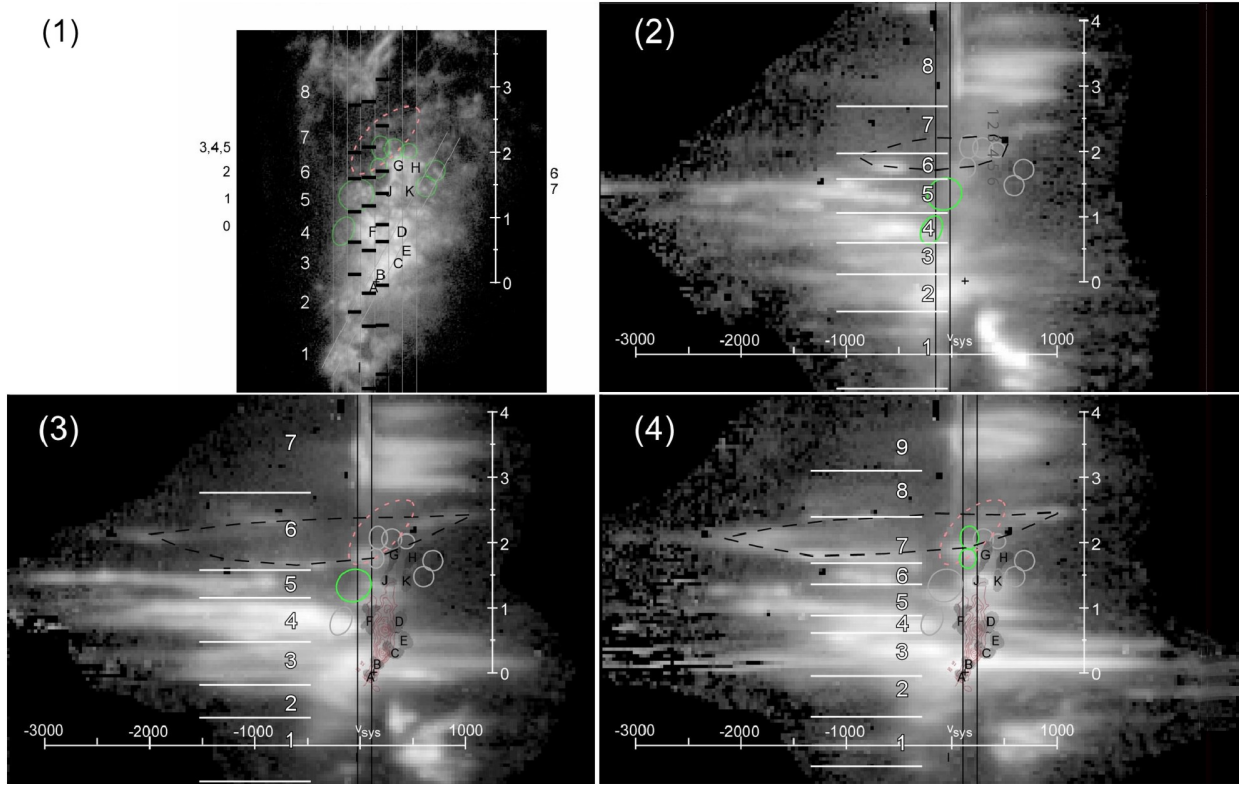[2]See www.stsci.edu/hst/stis/documents/handbook/currentIHB/images/c13_specrefa30.gif

Fig. 1.— Top left: FOC [O III] image of the NLR of NGC 1068 (Macchetto et al. 1994). The vertical scale is in arcseconds from the nucleus ($1'' = 70$ pc) and runs along P.A. 38° with NE at top. Slits used for UV spectra (e.g. Figure 2) are shown and numbered in gray, and the regions from which spectra in Figs. 3 & 4 are extracted are numbered. The other 3 panels show the [O III] emission-line profiles that we discussed in Paper I.
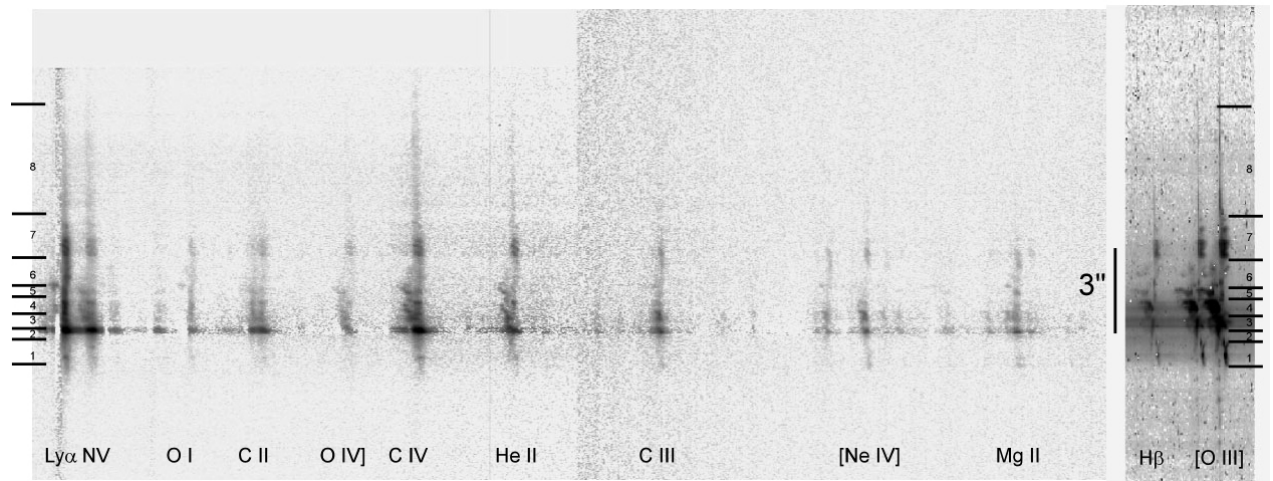

Fig. 2.— A continuum subtracted, STIS FUV+NUV spectrogram of NGC 1068, this one adjacent to the radio jet (panel 3 in Figure 1), using the $0''.2$-wide slit. The horizontal lines are those of Figure 1, and delineate the regions over which we averaged spectra (and are shown before continuum subtraction). The Hβ and [O III] profiles from Paper I have been rebinned to match the resolution of the UV data, and are shown before continuum subtraction. High-velocity features are evident on many of the lines. To fit everything on this plot, the wavelength scale is linear but discontinuous, and the intensities are log-scaled.

The STIS data processing pipeline delivered wavelength and flux calibrated spectra as well as the statistical error in flux at each pixel. We removed continuum light by averaging across line-free intervals, fitting the result with a low-order Chebyshev polynomial, and subtracting the fit from the data. To deredden spectra, we used the standard reddening curve of Mathis, Rumpl, & Nordsieck (1977) and estimates that KC derived from the He IIλ1640/λ4686 flux ratio along their single slit. KC found systematic differences between blue– and red–shifted emission, with gas in the NE–blue quadrant more heavily reddened ($E_{B-V} \sim 0.35$) than that in the NE–red quadrant (~ 0.22). Although they placed their slit along P.A. $22°$, rather than our $38°$, and displaced it $0\rlap{.}''14$ north of the continuum peak, we applied their values to all of our spectra because we could not include the He IIλ4686 line in our spectral maps. Figure 2 shows one of the three resulting FUV+NUV spectrograms. The blue wing of the strong Ly α line is invariably obliterated by geocoronal emission, so is ignored in this Figure and in our analysis.

To improve signal to noise ratios, we binned spectra into the spatial regions marked in Figure 1 and into velocity increments of 200 $\mathrm{km\,s}^{-1}$. These intervals were chosen to bracket distinct changes in kinematical behaviour and to encompass discrete radio knots. To link to our previous analysis, we rebinned the [O III] and Hβ spectra from Paper I to the spectral/spatial resolutions of the UV spectra; the two line sets are registered in Figure 2. Figure 3 compares the line profiles extracted from each spectrogram at each of these regions. Regions 1 and 2 contain the brightest emission from the base of the SW ionization cone, region 3 encompasses the nucleus and the base of the NE ionization cone so shows the brightest lines, while regions beyond show the profiles from kinematically distinct regions across the cone.

3. Results

Our spectra show the UV lines usually visible from a moderately reddened NLR, especially strong [Ne IV] and C IV nearest the nucleus. Note that the high velocity features on the detailed optical spectra in Figure 1 are also prominent on the UV lines — especially on the strongest three, He IIλ1640, C IV$\lambda\lambda$1549, and C III]λ1909. Each panel in Figure 3 compares these profiles at one spatial region and slit position. Slit 4, panel 3 covers the "continuum hotspot" discussed by Crenshaw & Kraemer (2000), and confirms the broad C IV line profile there, which Antonnuci, Hurt, & Miller (1994) found is polarized because it reflects emission from the hidden BLR. As discussed in Paper I, the spectra of many bright knots in other regions of the NLR also show evidence for a few percent contribution from nuclear light.

The axis of the ionization bicone lies close to the plane of the sky (Cecil, Bland, & Tully 1990, for example), about $45°$ above the galaxy disk. As well as picking up scattered nuclear light, our line of sight therefore penetrates a large range of gas densities and plausibly ionization conditions through the galaxy atmosphere, depending on whether the gas is in front of the jet (i.e. accelerating above the galaxy disk) or below it (i.e. decelerating into the denser galaxy disk). Line profiles throughout the NE cone have consistently stronger blue wings, indicating that NLR clouds

are being pushed laterally from the cone axis, toward us.

3.1. Models of Gaseous Excitation

We summarized the space and velocity variations in excitation in the diagnostic diagrams of ADT, plotting the ratios of C IV $\lambda\lambda1549$/He II $\lambda1640$ against C IV $\lambda\lambda1549$/C III] $\lambda1909$ (figure 4) These have been chosen because the three are among the strongest lines, their ratios are least affected by reddening uncertainties and the contribution of scattered nuclear light, and most clearly distinguish between photoionization and shock excitation. We used Monte Carlo techniques to estimate errors from the combined uncertainties of the continuum subtraction, velocity rebinning, dereddening (assuming a bump in its curve near $\lambda218$ nm), and the division of the different line profiles to form ratios. While there is evidence that reddening in this NLR is anomalous compared to both the Milky Way and the Magellanic Clouds (Antonnuci, Hurt, & Miller 1994), and dust is presumably also distributed within the densest clouds, the ratios chosen by ADT minimize such uncertainties. The arrow on panel (1) of figure 4 shows the effect of an external extinction of 3 A_V upon the models.

Figure 4 plots the observed flux ratios at various points in the NLR with the predictions of both shock and photoionization models. Data colors and symbols are explained in the plot caption. Each panel a–c is bissected, with the left panels comparing our spectra with shock models, and the right with photoionization models, which we now discuss.

3.1.1. Shock Models

We compared the data to two shock model grids from ADT: a pure shock only, and after addition of its photoionizing precursor; Dopita & Sutherland (1996) detail the model physics. Grids are labeled by shock speed and magnetic parameter (an ambient magnetic field inhibits shock compression). Essentially all the data points are clearly displaced from the shock grids. Increasing extinction by ~ 3 A_V beyond what we have used would bring many points into agreement with the shock predictions, but is unwarranted by other data.

3.1.2. Photoionization Models

We used the latest version of the shock/photoionization code MAPPINGS III (Groves, Dopita & Sutherland 2004a). Density and the spectral index α of the single ionizing power-law label our photoionization grids; using a structured, filtered ionizing continuum such as that of Alexander et al. (2000) produced similar results for our application. The final input is the ionization parameter U, which measures the number of ionizing photons per hydrogen atom at the inner surface of the
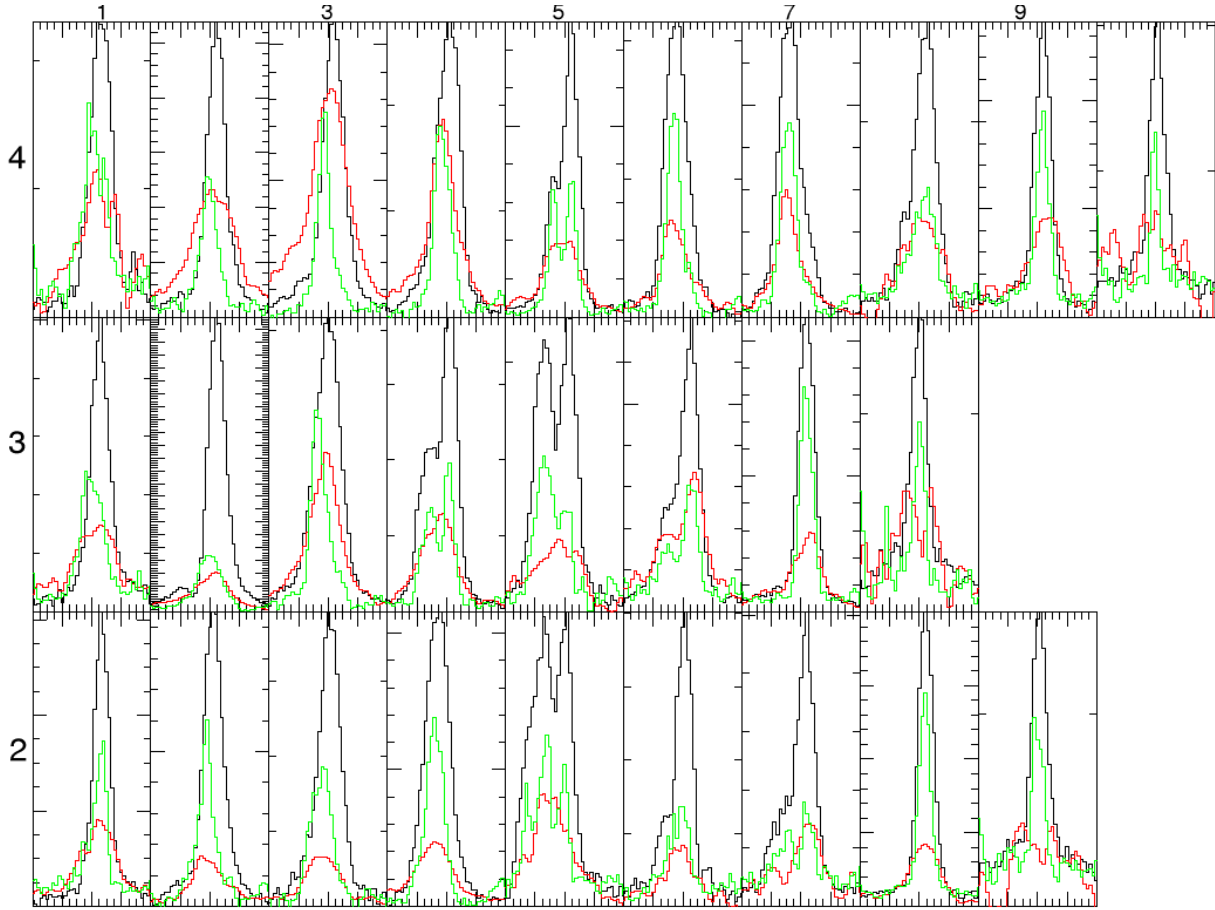
Fig. 3.— Emission-line profiles of (green) He II, (black) C IV, and (red) C III, are shown dereddened but otherwise unscaled. In the grid of spectra, slit number is vertical, and spatial interval across the NLR is horizontal and increases from SW at left region 1, the AGN in region 3 (of slit 3), into the NE cone toward the right. Small ticks are every 1000 $km\,s^{-1}$ in the full range of ± 9000 $km\,s^{-1}$, centered on galaxy systemic velocity.
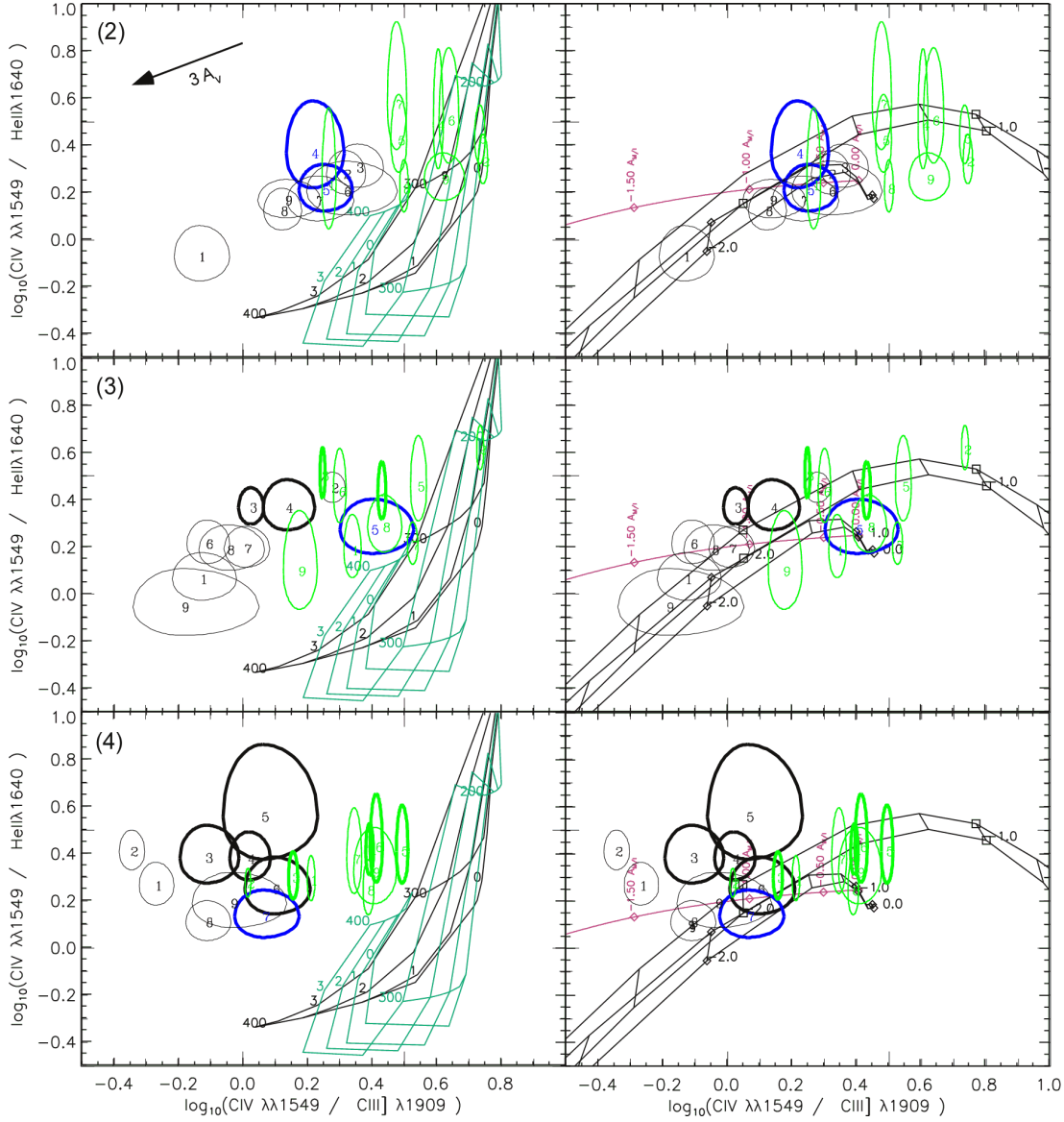
Fig. 4.— Flux ratios from dereddened STIS spectra across the NLR are compared to the results of (left columns) shock and (right columns) photoionization models. Panel a) contains the regions from slit (2), b) slit (3) and c) slit (4). The 2σ error ellipse from each pair of line ratios is numbered by its extraction region in Figure 1. Heavy ellipses correspond to the ratios at points coincident with the radio jet, while light ellipses corresponds to points off the jet. Black ellipses plot ratios of high-velocity gas (beyond $\pm 500\,\mathrm{km\,s^{-1}}$ of galaxy systemic), whereas green plot ratios for velocities within $\pm 500\,\mathrm{km\,s^{-1}}$ of systemic. The two models from ADT shown in the left-hand panels are for a pure shock and a shock+photoionizing precursor; both are labeled by the shock speed and magnetic parameter $B/\sqrt{n}$. Three photoionization models are shown in the right panels: the $A_{M/I}$ sequence varies the covering fraction of matter- to ionization-bound clouds. The other curves plot at top a single isochoric cloud, and at bottom an isobaric, dusty radiation pressure dominated cloud. Each model varies ionization parameter U from $\log U = -3.0$ to 0 in steps of 0.3 from right to left, at two values of the gas ([S II]) density $n = 10^2$ & 10^4 cm^{-3} in the case of the dusty model.

cloud. The right-hand panels of Figure 4 show three sequences of photoionization models:

1. A sequence of constant density, isochoric, ionization bounded clouds.

2. The $A_{M/I}$ sequence of Binette, Wilson, & Storchi-Bergmann (1996), which follows by combining the emission from two components: matter bounded clouds and ionization bounded clouds. The sequence is parameterized by the ratio of the solid angle occupied by the Matter bounded component to that of the Ionization bounded component.

3. A sequence of dusty, radiation pressure dominated clouds from Groves, Dopita & Sutherland (2004a,b). Each cloud is pressurized mostly by radiation while being exposed to the same input spectrum as the isochoric model. The cloud is therefore isobaric, so density here refers to the depth where H II = H I, approximately where [S II] is emitted, and U where the temperature reaches 2×10^4 K predominantly by photoelectric heating.

3.2. Line Ratio Diagrams

The first panel in figure 4 shows slit 2. The high velocity data points (black ellipses) are clustered within the same region of the Line diagnostic diagram. These points have too low C IV/C III] ratio to be reproduced by the shock data, but are in reasonable agreement to the photoionization data. The only discrepancy is from region 1 wish may be due to the low C IVand noise. The systemic (green ellipses) data points are more dispersed, with some in the same region as the high velocity clouds and the regions closest to the nucleus (2 and 3) having high C IV/C III] ratios. The regions with high C IV/C III] ratios are equally well represented as either shock excited clouds or regions with high ionization parameter.

Panel b) shows these slit #3 observations. These are similar to slit #2, but some observations (heavy ellipses) are coincident with the radio jet, as seen in figure 1. Compared to panel a), the clustering of the high velocity observations is at lower values of C IV/C III] and C IV/He II, and is not as tight, with the jet coincident observations having higher C IV/C III] values. However the majority of the high velocity points are still better reproduced by the photoionization models, with the jet coincident observation possibly containing some shock contribution. The systemic observations are again dispersed, with the nucleus dominated observation, region 2, showing the strongest C IV/C III] and C IV/He IIratios. The systemic observations with high C IV/C III] can possible be reproduced by shocks, but most require a dominant contribution by photoionization.

The slit #4 observations are shown in panel c), and again show the same clustering of the high velocity observations, slightly more dispersed and with lower C IV/C III] values than in panel a). The jet coincident observations again show higher C IV/C III] values, indicating the possible contribution by shocks to the emission. Though the photoionization models are an improvement over the shock models in reproducing the observations the ellipses are still significantly displaced from the models. This could possibly be due to much greater reddening, errors in the reduction

or observations, or different parameters in the clouds, such as a greater metallicity. The systemic observations in slit #4 show a greater clustering than in the previous slits. Regions 2, 3 and 4, which are coincident or close to the nucleus, have lower values of C IV/C III] than the other systemic observations, differing from the previous slits.

4. Discussion

In each panel of Figure 3, C IV is the strongest line, which indicates a high state of gaseous excitation.In addition, the emission in each region is brightest around systemic velocity. For gas accelerated from rest and excited by a shock front, one would expect the opposite trend: gas at the *highest* velocities would be moving closest to the shock, and hence would have greatest excitation.

In general, data in Figure 4 plot closer to photoionization than shock models. In particular, the last 3 panels of all slits in Figure 3 span the extended NLR beyond $2''$ radius, and show similar, red asymmetric line profiles and photoionized flux ratios. In contrast, the region 5 profiles from each slit are multipeaked and this region has enhanced X-ray emission (Young, Wilson, & Shopbell 2001). The [O III] image shows that this region is delineated by clusters of unresolved knots whose [O III] spectra (Figure 1) are very blueshifted and have large velocity dispersions. In §2, we noted that the velocity shifts produced by placing such compact features within the $0''.2$-wide slit would be only $\sim 10\%$ of those observed. Despite their kinematical discontinuities, these spectra also have much smaller C IV/C III] ratios than produced by the shock and shock+precursor models in Figure 4. This finding is consistent with the strong signature of photoionization in *Chandra* spectra (Kinkhabwala et al. 2002), and strong coronal-line emission evident in optical (Kraemer & Crenshaw 2000) and IR (Marconi et. al. 1996) spectra of the NE quadrant of the NLR between 1–$2''$ radii.

The photoionization model which is correct is not obvious in figure 4, but other line diagnostic diagrams may indicate better the correct model (Groves, Dopita & Sutherland 2004b).

4.1. Effect of the Radio Jet

Comparing Figures 1 and 3, we looked for correlated changes in gaseous excitation and kinematics that might signify shocks. Such shock signatures could possibly arise through jet-cloud interactions. We spanned the SW half of the jet with slit 4 (slit 5 spanned its NE half but only in the NUV, preventing us from deriving interesting line ratios). Regions 3–5 include some posited jet/ISM interaction sites. Across region 3 the [O III] profiles in Figure 1 panel (4) straddle systemic velocity. Although the [O III] profiles span in excess of ± 2000 km s^{-1}, both carbon ions have a broad blue wing centered around -3500 km s^{-1} from systemic velocity; this feature is associated with cloud B and coincides both with the UV continuum "hotspot" of scattered nuclear light, and with the posited jet/ISM interaction of Gallimore, Baum, & O'Dea (1996). Despite these large

velocities, the UV profiles show excitation changes only around systemic velocity where C IV is about 50% stronger than C III]. In fact, the flux ratios of the blue and red wings are among the farthest points from the shock grids in Figure 4.

4.2.   Radiative Acceleration

We therefore confirm that UV/optical gas in this ionization cone is not dominated by shocks. How, then, are such compact knots accelerated to high velocities without disintegrating? In Paper I §4.3.4 we explored radiative acceleration of *dusty* clouds, and detailed this idea in Dopita et al. (2002). The radiative force photoablates gas+dust from the surface of the NLR cloud, driving it away from the ionizing source (see Figure 1 in Dopita et al. 2002). Because much of the ionizing opacity at high U is from dust that is coupled tightly to the gas by Coulomb interactions, this force can be appreciable and really applies to the cloud as a whole. At the edges of NLR clouds there is no counteracting pressure gradient, and the full radiative force accelerates this gas from the active nucleus. Such a model is supported by Galliano et al. (2003), who conclude that the dust in the NLR is probably distributed in optically thick dust clouds, as pictured in our idea.

As pointed out by Kraemer & Crenshaw (2000), during its outflow the high velocity tail of the NLR clouds will be shielded from ionization by the lower velocity flow that feeds the ionizing central source. Just such an ionization gradient is seen in Figure 4, where both blue- and redshifted components have smaller C IV/C III] ratios than the systemic components; this trend would arise if the high velocity flows see a lower U, perhaps from a filtered continuum (as posited by Alexander et al. 2000), compared to that of the systemic component.

4.3.   Are the Knots Related to Associated Absorbers?

As mentioned in Paper I, if the high velocity emission knots were seen in absorption against the nucleus instead of in emission against the galaxy disk, their kinematics would resemble those of associated absorption line (AAL) systems. We have now shown that their UV spectra also resemble the ionization structure of AAL's in that both have strong UV resonance lines O VI, N V, C IV, Mg II, and Si II (Hamann et. al. 1997, for example for AAL's). The high-velocity knots in this NLR may, therefore, be resolved AALs seen in emission.

An important test of this hypothesis would be to determine the column density and total masses of the knots. Where measurable and unsaturated, the columns of AAL's are $N_H = 10^{19}$ to $> 10^{20}$ cm^{-2} in moderately ionized regions. This gas is thought to arise from an accretion disk wind, and scaling of the C IV equivalent width with increasing UV luminosity ("Baldwin effect") has been interpreted as evidence for a radiation–pressure driven outflow (Vestergaard 2003). Well studied AAL's often show even more highly ionized X-ray absorption (George et al. 1998; Crenshaw et al. 1999, for example), but their distance to the galaxy nucleus is poorly constrained by UV line

variability and excited-state density diagnostics, so results are highly uncertain.

Present constraints on masses (Cecil et al. 2002) for the bright knots in NGC 1068 assume case-B recombination conditions, hence limit only the ionized mass to typical values 5–10 $M_\odot/(10^4$ cm^{-3}). However, the blueshifted clouds are $0\rlap{.}''5$–$1\rlap{.}''7$ NE of the nucleus, so integral field optical/IR spectral maps can constrain cloud columns and total masses in a straightforward fashion. Such spectra would further constrain the physical properties of the high-velocity NLR clouds by mapping ionized gas density, temperature, and U gradients, and would have the potential to clarify properties of unresolved quasar AAL's and radiatively accelerated outflows in general.

5. Conclusions

Like the [O III] spectra presented in Paper I, *HST* UV spectral maps of the NLR of NGC 1068 show bright regions of emission that have been accelerated to velocities greater than 3000 km s^{-1} relative to adjacent gas. Knot excitation is not influenced directly by the radio jet. Our photoionization models reproduce the flux ratios of the strongest UV emission lines across the NLR much better than the shock models. With no indication of shock interaction, the high velocity knots are certainly photoionized, and may be radiatively accelerated, photoablata from NLR clouds. They show the same ionization and kinematical structure as the associated absorbers seen in a few percent of quasar spectra, hence may provide us with a unique opportunity to resolve a fundamental aspect of quasar dynamics: radiative acceleration of dusty clouds by the AGN.

REFERENCES

Alexander, T., Lutz, D., Sturm, E., Genzel, R., Sternberg, A., & Netzer, H. 2000, ApJ, 536, 710

Allen, M. G., Dopita, M. A., & Tsvetanov, Z. I. 1998, ApJ, 493, 571

Antonnuci, R. R. J., Hurt, T., & Miller, J. 1994, ApJ, 430, 210

Axon, D. J., Marconi, A., Capetti, A., Macchetto, F. D., Schreier, E. A., & Robinson, A. 1998, ApJ, 496, L75

Binette, L., Wilson, A. S., & Storchi-Bergmann, T. 1996, A&A, 312, 365

Capetti, A., Axon, D. J., & Machetto, F. D. 1997, ApJ, 487, 560

Cecil, G., Bland, J., & Tully, R. B. 1990, ApJ, 355, 70

Cecil, G., Dopita, M. A., Groves, B., Wilson, A. S., Ferruit, P., Pécontal, E., & Binette, L. 2002, ApJ, 568, 627 (Paper I)

Crenshaw, M. et al. 1999, ApJ, 516, 750

Crenshaw, M. & Kraemer, S. 2000, ApJ, 532, 247

Dopita, M. A., Groves, B. A., Sutherland, R. S., Binette, L., & Cecil, G. 2002, ApJ, 572, 753

Dopita, M. A. & Sutherland, R. S. 1996, ApJS, 102, 161

Galliano, E., Alloin, D., Granato, G. L., & Villar-Martín, M. 2003, A&A, 412, 615

Gallimore, J. F., Baum, S. A., & O'Dea, C. P. 1996, ApJ, 464, 198

George, I. et al. 1998, ApJS, 114, 73

Grimes, J. P., Kriss, G. A., & Espey, B. R. 1999, ApJ, 526, 130

Groves, B., Dopita, M., & Sutherland, R. 2004a, ApJS, submitted

Groves, B., Dopita, M., & Sutherland, R. 2004b, ApJS, submitted

Hamann, F., Barlow, T. A., Junkkarinen, V., & Burbidge, E. M. 1997, ApJ, 478, 80

Kinkhabwala, A. et al. 2002, ApJ, 575, 732

Kraemer, S. B. & Crenshaw, M. 2000, ApJ, 532, 256 (KC00)

Machetto, D., Capetti, A., Sparks, W. B., Axon, D. J., & Boksenberg, A. 1994, ApJ, 435, 15

Marconi, A., van der Werf, P. P., Moorwood, A. F. M., & Oliva, E. 1996, A&A, 315, 335

Mathis, J. S., Rumpl, W., & Nordsieck, K. H 1977, ApJ, 217, 425

Nelson, C. H. & Whittle, M. 1996, ApJ, 465, 96

Pécontal, A., Ferruit, P., Binette, L., & Wilson, A. S. 1997, Ap&SS, 248, 167

Veilleux, S., & Osterbrock, D. E. 1987, ApJS, 63, 295

Vestergaard, M. 2003, ApJ, 599, 116

Young, A. J., Wilson, A. S., & Shopbell, P. L. 2001, ApJ, 556, 6